

# MonoForce: Learnable Image-conditioned Physics Engine

Ruslan Agishev\*, Karel Zimmermann\*

**Abstract**—We propose a novel model for the prediction of robot trajectories on rough offroad terrain from the onboard camera images. This model enforces the laws of classical mechanics through a physics-aware neural symbolic layer while preserving the ability to learn from large-scale data as it is end-to-end differentiable. The proposed hybrid model integrates a black-box component that predicts robot-terrain interaction forces with a neural-symbolic layer. This layer includes a differentiable physics engine that computes the robot’s trajectory by querying these forces at the points of contact with the terrain. As the proposed architecture comprises substantial geometrical and physics priors, the resulting model can also be seen as a learnable physics engine conditioned on real images that delivers  $10^4$  trajectories per second. We argue and empirically demonstrate that this architecture reduces the sim-to-real gap and mitigates out-of-distribution sensitivity. The differentiability, in conjunction with the rapid simulation speed, makes the model well-suited for various applications including model predictive control, trajectory shooting, supervised and reinforcement learning, or SLAM. The codes and data are publicly available<sup>1</sup>.

**Index Terms**—Robot-terrain Interaction, Differentiable Physics, End-to-end Learning, Monocular Vision, Trajectory Prediction

## I. INTRODUCTION

Autonomous robotics in off-road environments holds immense promise for various commercial applications, including outdoor logistics, inspections, and forestry operations. Yet, unlike systems designed for controlled environments, such as factories, off-road autonomous systems still remain prohibitively immature for dependable deployment. The main challenge that prevents reliable off-road deployment lies in the inability to predict the behavior accurately of the robot on the terrain. For example, the prediction of robot trajectory in tall vegetation or muddy and rocky terrains, especially from camera images and lidar scans, remains an unresolved problem in outdoor robotics.

Over the last decade, roboticists proposed a wide variety of *white-box* [1], [2], [3] and *black-box* models [4], [5], [6], [7], [8] for the off-road trajectory prediction. Black-box models primarily suffer from a severe out-of-distribution problem – the phenomenon where the distribution of training data does not correspond to the testing data. This problem naturally arises from the fact that the training data includes only the trajectories from safe terrain traversals, such as small terrain steps, while the decision about terrain traversability also naturally comprises the non-traversable terrains, such as tall cliffs, **Figure 4**. Since the step-to-cliff-generalization of large state-of-the-art black-box models is typically poor, the

\*The authors are with the VRAS group, Faculty of Electrical Engineering, Czech Technical University in Prague, Czech Republic (e-mail: agishrus@fel.cvut.cz; zimmerk@fel.cvut.cz) (Corresponding author: R. Agishev.)

<sup>1</sup><https://github.com/ctu-vras/monoforce>

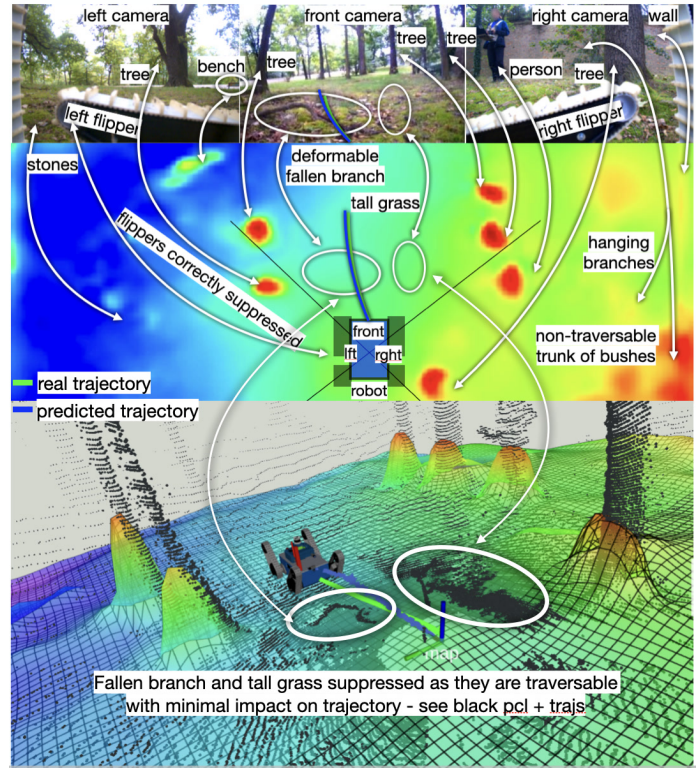


Fig. 1. **Qualitative results:** The first three rows show (i) onboard camera images (the only input), (ii) predicted supporting terrain and (iii) a 3D view with predicted trajectory and visualized ground truth lidar point clouds (not used for estimation). While the majority of rigid objects are correctly reconstructed from the camera image, robot flippers, tall grass, fallen branches, or soft hanging branches are correctly suppressed as they do not influence the resulting robot trajectory. Predicted terrain friction, dampening, and stiffness are not visualized for brevity.

safety of the resulting system is arbitrarily inferior. On the other hand, *white-box* architectures offer good generalization due to substantial inductive bias but often suffer from the sim-to-real gap – the phenomenon where a model “trained in” or “replaced by” simulation faces challenges or discrepancies when applied in the real world. Although several techniques, such as rapid motor adaptation [9], are known to partially suppress this issue through domain randomization, the sim-to-real gap, as well as the out-of-distribution problem, makes trajectory prediction from camera images prohibitively unreliable. We introduce a *grey-box* model that combines the best of both worlds to achieve better generalization and a smaller sim-to-real gap. This model enforces white-box laws of classical mechanics through a physics-aware neural symbolic layer, while preserving the ability to learn from huge data as it is end-to-end differentiable. We demonstrate that even just a single onboard camera is enough for reliable autonomous deployment in off-road environments; see Figures 1, 3 for some qualitative

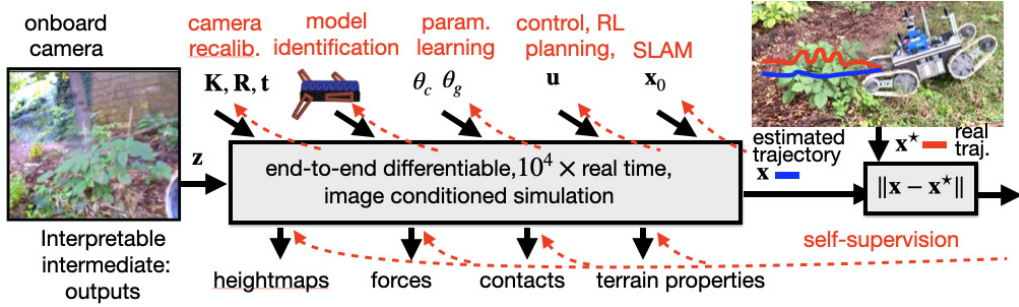


Fig. 2. **Model overview:** The proposed model can be seen as an image-conditioned differentiable simulation that delivers a million simulated trajectories per second on the terrain depicted in the onboard camera image. The explainable structure also delivers many intermediate interpretable outputs that can serve for efficient self-supervision.

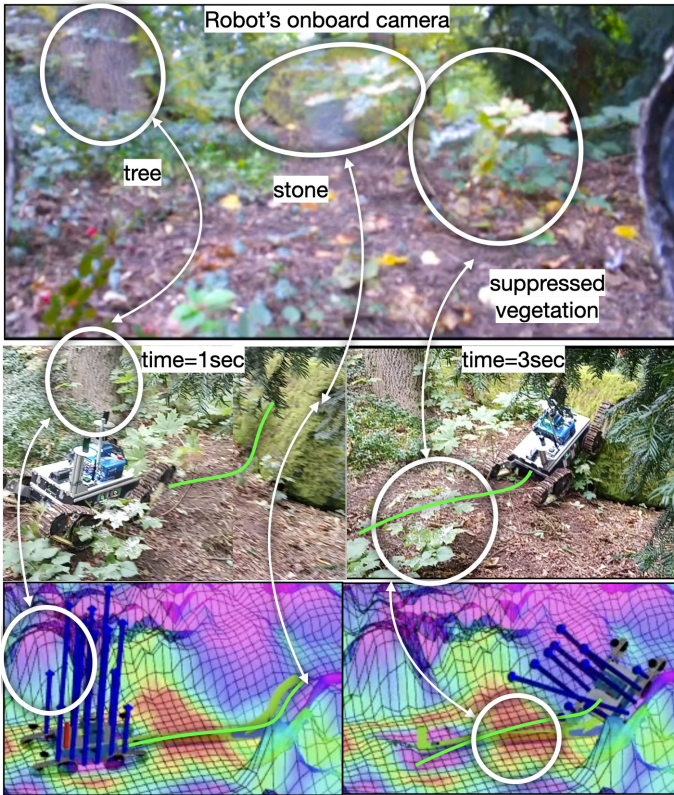


Fig. 3. **Qualitative results:** Given input onboard image from the robot’s camera (first row), the method distinguishes stones and trees as obstacles, while vegetation is suppressed (see 3D view in third row) the stone is preserved despite having almost the same green color as vegetation due to the moss coverage. Heightmap color encodes predicted terrain friction, and dark blue arrows show predicted contact forces. The predicted robot trajectory is visualized in light green. The ground truth robot motion is captured in the second row.

results and Figure 5 for quantitative evaluation.

We highlight that all state-of-the-art models, including the proposed one, are inherently statistically inconsistent as it is impossible to provide training data covering dangerous cases. Consequently, providing a close-to-infinite number of training examples, as typical, for large foundation models [10] does not imply a superior performance. Addressing the statistical inconsistency for the trajectory prediction task without resorting to real-world robot-damaging trajectories remains an

open challenge. In this work, we make a step toward this direction by introducing a grey-box model that leverages: (i) the strengths of black-box models to learn effectively from real data, thereby reducing the sim-to-real gap, and (ii) the strengths of white-box approaches to generalize effectively to unseen data, thereby addressing the out-of-distribution problem.

In our implementation, the black-box model predicts robot-terrain interaction forces and the shape of the robot-supporting terrain, while the neural symbolic layer, which contains a differentiable physics engine, solves the robot’s trajectory by querying these forces at the robot-terrain contacts. The main advantage of this approach is that it enables further self-supervision induced by lidar measurements, which essentially provides an upper bound on the terrain shape. Since lidar measurements are not restricted to safe terrains, the prediction of the shape remains statistically consistent. If we could further assume that terrain textures on unsafe terrains also appear on safe terrains, the whole procedure would be statistically consistent. However, this is not true in general, as there could be some inherently unsafe textures, such as holes covered by vegetation, which do not have their safe counterpart.

As the proposed architecture comprises substantial geometrical and physics priors, the resulting model can be also seen as *learnable physics engine conditioned by a real image* that delivers  $10^4$  trajectories per second; see Figure 2 for details (the engine efficiency is also investigated in the Section IV-D). In addition to that, the model is end-to-end-differentiable; therefore, gradients can be backpropagated towards its (i) convolutional filters, (ii) camera and robot parameters, (iii) control, (iv) positions, and (v) terrain properties. The differentiability, in conjunction with the rapid simulation speed, makes the model suitable for a myriad of tasks, including model predictive control [11], trajectory shooting [12], supervised and reinforcement learning [13], SLAM [14], online robot-model reidentification or camera recalibration [15]. The explainable structure of the proposed architecture also delivers a variety of intermediate outputs, such as terrain shape and its physical properties, robot-terrain reaction forces or contact points, which can all serve as efficient sources of self-supervision if measured during the training set creation or restricted in PINN-like manner [16]. We observed that the instability of gradient computation in existing differentiable simulators, such

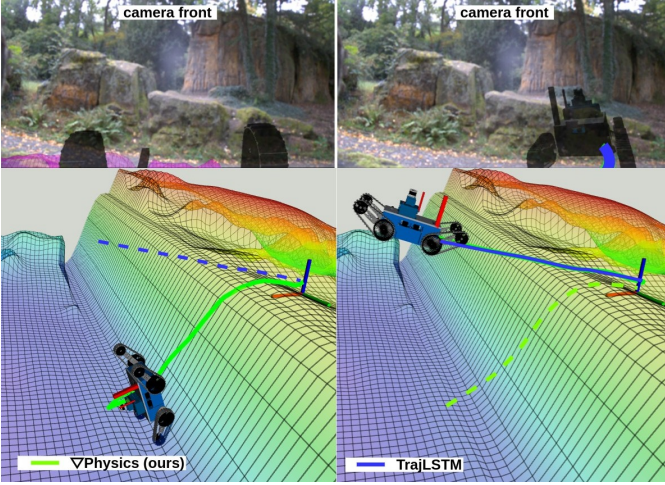


Fig. 4. **Generalization to robot-endangering scenarios** (non-present in dataset). Qualitative example of trajectory predictions with  $\nabla$ Physics and TrajLSTM (data-driven) models. The robot starts at the edge of a cliff and is given a command to move forward. **Left:** robot-terrain interaction prediction with  $\nabla$ Physics model (a correct estimate of falling down). **Right:** robot-terrain interaction prediction with TrajLSTM [19] model (incorrect prediction of hovering over a cliff as the robot-endangering situations are typically not present in datasets).

as NVIDIA’s WARP [17] and Google’s BRAX [18], makes them prohibitively unreliable and slow for both the learning and the inference. As a suitable replacement, we introduce a differentiable neural symbolic layer, which involves our from-scratch implemented physics engine, into the proposed architecture. This solution outperforms existing works in gradient stability and computational speed while preserving sufficient accuracy for reliable trajectory prediction. As all target applications, including learning, control, planning, and SLAM, can be naturally parallelized, we also achieve significant speed-up through massive parallelization on GPU.

**Our main contributions** are as follows.

**Step towards statistically consistent learning:** Explainability of the proposed grey-box model provides several well-interpretable intermediate outputs that serve as a natural source of self-supervision. The self-supervision, hand in hand with a substantial physical prior, increases the statistical consistency of the learning procedure.

**Image-conditioned simulation:** The end-to-end differentiable image-conditioned simulation is suitable for a myriad of robotics tasks such as control or SLAM, as it predicts  $10^4$  trajectories in parallel per second.

**Experimental evaluation on non-rigid terrains:** The proposed model outperforms other state-of-the-art methods on non-rigid terrains, such as grass or soft undergrowth that deforms when traversed by the robot. See Figure 5 for quantitative results.

## II. RELATED WORK

### A. Black-box (Data-driven) Models

The environment representation modeling from a single [23] or multiple RGB images [20] in a top-down view has been

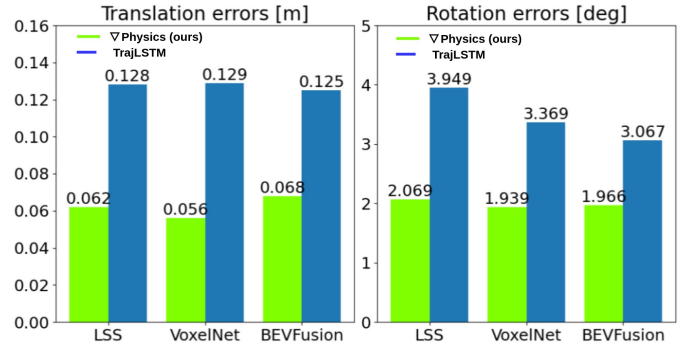


Fig. 5. **Generalization and results:** The proposed neuro-symbolic layer  $\nabla$ Physics generalizes to out-of-distribution examples well. The overall results are consistently better independent of the architecture (LSS [20], VoxelNet [21], BEV-Fusion [22]) used for terrain properties estimation.

widely studied in the literature. The geometry of the scene prediction (taking into account occlusions) from stereo or depth-camera input has been addressed in [24]. The importance and benefits of sensor fusion (camera images, lidar, and radar) for environment representation have been demonstrated in [25]. The authors of RoadRunner [26] developed an end-to-end learning-based framework that predicts the traversability and elevation maps from multiple images and a lidar voxel map. However, the robot-terrain interaction and trajectory prediction tasks are not considered in these works.

The Recurrent Neural Networks (RNN) models [27] and especially their variant Long Short-Term Memory (LSTM) [28] and Gated Recurrent Unit (GRU) [29] have been widely and successfully used [30], [31], [19] for trajectory prediction tasks of various agents (mobile robots, cars, airplanes, people, and more). However, their main drawback lies in the difficulty of capturing the underlying physical laws, which leads to limited generalization capabilities (more in Section III-C and Figure 4).

### B. White-box (Physics-based) Models

The vehicle-terrain interaction modeling and traction mechanics have been widely studied in the literature [33], [34]. To provide accurate analysis and prediction of off-road vehicles behavior on the terrain, a set of high-fidelity physics-based software tools have been developed. For example, Vortex Studio [35] allows for realistic wheeled and tracked locomotion simulations and extensive land and even planetary environment modeling. The Chrono [36] is a physics-based engine designed for ground vehicle-tire-terrain interactions simulation. It supports the integration of various vehicle and tire models and can simulate deformable terrain. The AGX physics engine (more specifically, its terrain dynamics model *agxTerrain*) [37] enables simulation of soil dynamics and interactions with heavy vehicles. This software delivers realistic, high-fidelity simulations for applications involving complex soil-tool interactions. However, the mentioned physics engines are not differentiable, which makes them unsuitable for end-to-end learning and integration of exteroceptive real sensor data.

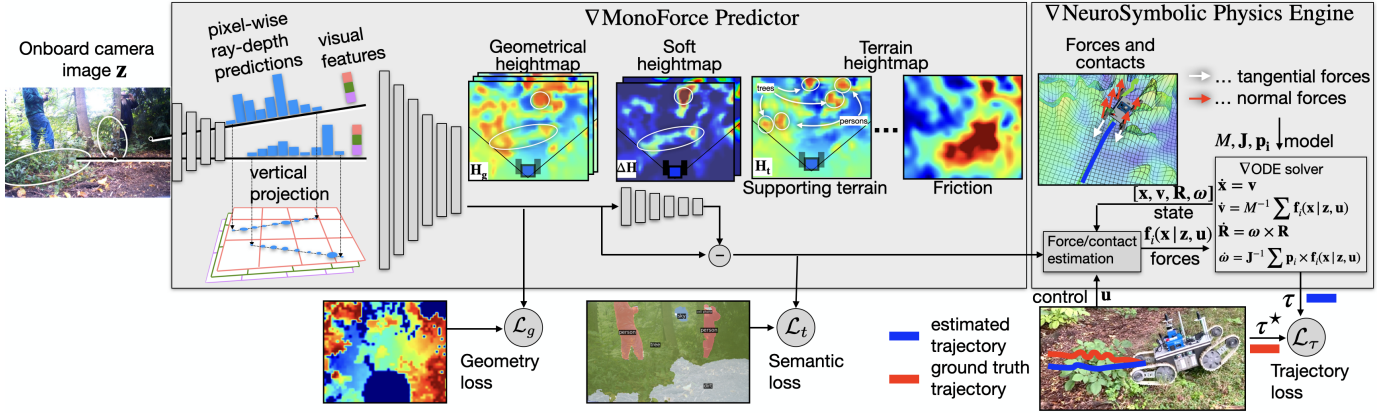


Fig. 6. **Detailed architecture overview:** Our model consists of a data-driven *Terrain Encoder* and physics-driven differentiable *Physics Engine*. The *Terrain Encoder* includes the adapted LSS [20] model (that transforms weighted depth predictions and rich visual features for each pixel ray to vertically projected 2.5D representation) and task-specific convolutional heads (that generate different terrain properties). The terrain properties contain the geometrical heightmap  $\mathcal{H}_g$ , the heights of the rigid layer of terrain hidden under the vegetation,  $\mathcal{H}_t = \mathcal{H}_g - \Delta\mathcal{H}$ , friction, stiffness, and dampening. Inside the  $\nabla$ *Physics engine*, given state, control, and terrain properties, forces at robot-terrain contacts are estimated. Finally, these forces are integrated to estimate the resulting robot trajectory. Learning employs three losses: *trajectory loss*,  $\mathcal{L}_\tau$ , which measures the distance between the predicted and real trajectory; *geometrical loss*,  $\mathcal{L}_g$ , which measures the distance between the predicted geometrical heightmap and lidar-estimated heightmap; *terrain loss*,  $\mathcal{L}_t$ , which enforces rigid terrain on rigid semantic classes revealed through image foundation model (SEEM [32]).

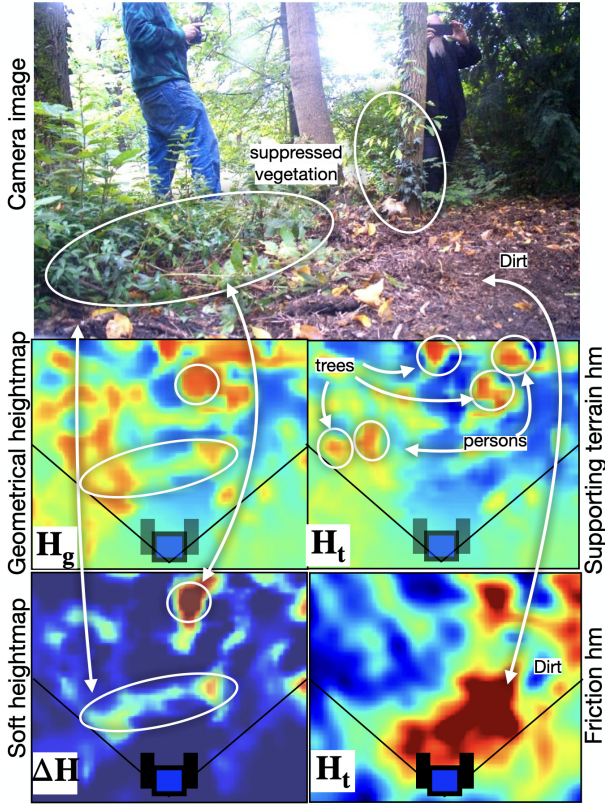


Fig. 7. **Detailed view of MonoForce's heightmaps:** Geometrical heightmap replicates lidar heightmap. Soft heightmap outlines soft parts of the terrain (those that do not generate any robot-terrain interaction forces) such as vegetation. Terrain heightmap consists of two layers: (i) Supporting terrain: geometrical heightmap with subtracted soft parts of the terrain; (ii) Friction heightmap: see significantly higher values on dirt.

### C. Grey-box (Hybrid) Models

To achieve the accuracy and efficiency of data-driven methods and at the same time to maintain the generaliza-

tion capabilities of the physics-based models, the *hybrid* approaches have been developed for off-road navigation. The PIAug [38] is a physics-informed data augmentation methodology designed to enhance the learning of vehicle dynamics, particularly in scenarios involving high-speed and aggressive maneuvers. The robot's motion prediction in off-road scenarios is the main focus of the work, however, the accuracy of terrain properties estimation is not addressed there. The PhysORD [39] is a promising neuro-symbolic model; the authors utilize neural networks to estimate the potential energy of a vehicle and external forces acting on it during the terrain traversal. The Hamiltonian and Lagrangian mechanics laws are then used to predict the vehicle dynamics. However, the integration of exteroceptive sensors (camera images and terrain properties) is not implemented there, limiting the deployment of the method in real-world off-road scenarios.

Building on the preceding works [40], [41], we support the integration of other sensor modalities, such as lidar (Section IV-B), into the MonoForce model, improve the accuracy of the physics engine (in terms of trajectory prediction, Figure 5) by using a precise robot model, expand the data sequences (Section IV-A) that are used to train the model focusing on tracked robots and more challenging navigation scenarios (low traction, diverse terrain inclinations, etc), and perform benchmarking against data-driven baselines (Section IV-C).

## III. METHOD

A detailed overview of the proposed architecture that converts images and control commands into trajectories is depicted in Figure 6. The model consists of several learnable modules that deeply interact with each other. The *terrain encoder* carefully transforms visual features from the input image into the heightmap space using known camera geometry. The resultant heightmap features are further refined into interpretable physical quantities that capture properties of the

terrain such as its shape, friction, stiffness, and damping. Next, the *physics engine* combines the terrain properties with the robot model, robot state, and control commands and delivers reaction forces at points of robot-terrain contacts. It then solves the equations of motion dynamics by integrating these forces and delivers the trajectory of the robot. Since the complete computational graph of the feedforward pass is retained, the backpropagation from an arbitrary loss, constructed on top of delivered trajectories, or any other intermediate outputs is at hand.

### A. Terrain Encoder

The part of the MonoForce architecture (Figure 6) that predicts terrain properties  $\mathbf{m}$  from sensor measurements  $\mathbf{z}$  is called *terrain encoder*. The proposed architecture starts by converting pixels from a 2D image plane into a heightmap with visual features. Since the camera is calibrated, there is a substantial geometrical prior that connects heightmap cells with the pixels. We incorporate the geometry through the Lift-Splat-Shoot architecture [20]. This architecture uses known camera intrinsic parameters to estimate rays corresponding to particular pixels – pixel rays, Figure 13. For each pixel ray, the convolutional network then predicts depth probabilities and visual features. Visual features are vertically projected on a virtual heightmap for all possible depths along the corresponding ray. The depth-weighted sum of visual features over each heightmap cell is computed, and the resulting multichannel array is further refined by deep convolutional network to estimate the terrain properties  $\mathbf{m}$ .

The terrain properties include the geometrical heightmap  $\mathcal{H}_g$ , the heights of the terrain supporting layer hidden under the vegetation  $\mathcal{H}_t = \mathcal{H}_g - \Delta\mathcal{H}$ , terrain friction  $\mathcal{M}$ , stiffness  $\mathcal{K}$ , and dampening  $\mathcal{D}$ . The intuition behind the introduction of the  $\Delta\mathcal{H}$  term is that  $\mathcal{H}_t$  models a partially flexible layer of terrain (e.g. mud) that is hidden under flexible vegetation, Figure 7.

### B. Differentiable Physics Engine

The differentiable physics engine solves the robot motion equation and estimates the trajectory corresponding to the delivered forces. The trajectory is defined as a sequence of robot states  $\tau = \{s_0, s_1, \dots, s_T\}$ , where  $\mathbf{s}_t = [\mathbf{x}_t, \mathbf{v}_t, R_t, \boldsymbol{\omega}_t]$  is the robot state at time  $t$ ,  $\mathbf{x}_t \in \mathbb{R}^3$  and  $\mathbf{v}_t \in \mathbb{R}^3$  define the robot's position and velocity in the world frame,  $R_t \in \mathbb{R}^{3 \times 3}$  is the robot's orientation matrix, and  $\boldsymbol{\omega}_t \in \mathbb{R}^3$  is the angular velocity. To get the next state  $\mathbf{s}_{t+1}$ , in general, we need to solve the following ODE:

$$\dot{\mathbf{s}}_{t+1} = f(\mathbf{s}_t, \mathbf{u}_t, \mathbf{z}_t) \quad (1)$$

where  $\mathbf{u}_t$  is the control input and  $\mathbf{z}_t$  is the environment state. In practice, however, it is not feasible to obtain the full environment state  $\mathbf{z}_t$ . Instead, we utilize terrain properties  $\mathbf{m}_t = [\mathcal{H}_t, \mathcal{K}_t, \mathcal{D}_t, \mathcal{M}_t]$  predicted by the terrain encoder. In this case, the motion ODE (1) can be rewritten as:

$$\dot{\mathbf{s}}_{t+1} = \hat{f}(\mathbf{s}_t, \mathbf{u}_t, \mathbf{m}_t) \quad (2)$$

Let's now derive the equation describing the state propagation function  $\hat{f}$ . The time index  $t$  is omitted further

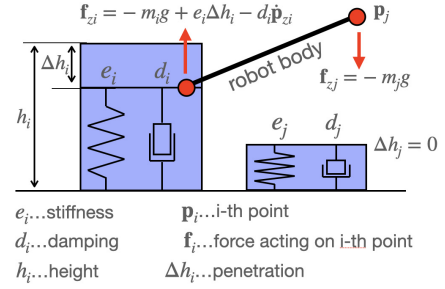


Fig. 8. **Terrain force model:** Simplified 2D sketch demonstrating normal reaction forces acting on a robot body consisting of two points  $p_i$  and  $p_j$ .

for brevity. We model the robot as a rigid body with total mass  $m$  represented by a set of mass points  $\mathcal{P} = \{(\mathbf{p}_i, m_i) \mid \mathbf{p}_i \in \mathbb{R}^3, m_i \in \mathbb{R}^+, i = 1 \dots N\}$ , where  $\mathbf{p}_i$  denotes coordinates of the  $i$ -th 3D point in the robot's body frame. We employ common 6DOF dynamics of a rigid body [42] as follows:

$$\begin{aligned} \dot{\mathbf{x}} &= \mathbf{v} & \dot{R} &= \Omega R \\ \dot{\mathbf{v}} &= \frac{1}{m} \sum_i \mathbf{F}_i & \dot{\boldsymbol{\omega}} &= \mathbf{J}^{-1} \sum_i \mathbf{p}_i \times \mathbf{F}_i \end{aligned} \quad (3)$$

where  $\Omega = [\boldsymbol{\omega}]_{\times}$  is the skew-symmetric matrix of  $\boldsymbol{\omega}$ . We denote  $\mathbf{F}_i \in \mathbb{R}^3$  a total external force acting on  $i$ -th robot's body point. Total mass  $m = \sum_i m_i$  and moment of inertia  $\mathbf{J} \in \mathbb{R}^{3 \times 3}$  of the robot's rigid body are assumed to be known static parameters since they can be identified independently in laboratory conditions. Note that the proposed framework allows backpropagating the gradient with respect to these quantities, too, which makes them jointly learnable with the rest of the architecture. The trajectory of the rigid body is the iterative solution of differential equations (3), that can be obtained by any ODE solver for given external forces and initial state (pose and velocities).

When the robot is moving over a terrain, two types of external forces are acting on the point cloud  $\mathcal{P}$  representing its model: (i) gravitational forces and (ii) robot-terrain interaction forces. The former is defined as  $m_i \mathbf{g} = [0, 0, -m_i g]^T$  and acts on all the points of the robot at all times, while the latter is the result of complex physical interactions that are not easy to model explicitly and act only on the points of the robot that are in contact with the terrain. There are two types of robot-terrain interaction forces: (i) normal terrain force that prevents the penetration of the terrain by the robot points, (ii) tangential friction force that generates forward acceleration when the tracks are moving, and prevents side slippage of the robot.

#### Robot-terrain interaction forces

##### Normal reaction forces.

One extreme option is to predict the 3D force vectors  $\mathbf{F}_i$  directly by a neural network, but we decided to enforce additional prior assumptions to reduce the risk of overfitting. These prior assumptions are based on common intuition from the contact dynamics of flexible objects. In particular, we assume that the magnitude of the force that the terrain exerts on the point  $\mathbf{p}_i \in \mathcal{P}$  increases proportionally to the deformation of



robot’s trajectories lie within the heightmap area, we use the shared heightmap input for all the LSTM units of the network. So the heightmap is processed through the convolutional layers **once** and flattened, producing a fixed-size spatial feature vector. This design choice (of not processing the heightmaps at different time moments) is also motivated by computational efficiency reason. At each moment  $t$ , this heightmap vector is concatenated with the fused spatial-control features and processed by an LSTM unit. The LSTM unit output for each timestep  $t$  is passed through a fully connected (dense) layer to produce the next state  $\mathbf{x}_{t+1}$ . The sequence of states form the predicted trajectory,  $\{\mathbf{x}_0, \dots, \mathbf{x}_T\}$ .

#### D. End-to-end Learning

Self-supervised learning of the proposed architecture minimizes three different losses:

**Trajectory loss** that minimizes the difference between SLAM-reconstructed trajectory  $\tau^*$  and predicted trajectory  $\tau$ :

$$\mathcal{L}_\tau = \|\tau - \tau^*\|^2 \quad (8)$$

**Geometrical loss** that minimizes the difference between ground truth lidar-reconstructed heightmap  $\mathcal{H}_g^*$  and predicted geometrical heightmap  $\mathcal{H}_g$ :

$$\mathcal{L}_g = \|\mathbf{W}_g \circ (\mathcal{H}_g - \mathcal{H}_g^*)\|^2 \quad (9)$$

$\mathbf{W}_g$  denotes an array selecting the heightmap channel corresponding to the terrain shape.

**Terrain loss** that minimizes the difference between ground truth  $\mathcal{H}_t^*$  and predicted  $\mathcal{H}_t$  supporting heightmaps containing rigid objects detected with Microsoft’s image segmentation model SEEM [32], that is derived from Segment Anything foundation model [46]:

$$\mathcal{L}_t = \|\mathbf{W}_t \circ (\mathcal{H}_t - \mathcal{H}_t^*)\|^2 \quad (10)$$

$\mathbf{W}_t$  denotes the array selecting heightmap cells that are covered by rigid materials (e.g. stones, walls, trunks), and  $\circ$  is element-wise multiplication.

Since the architecture **Figure 2** is end-to-end differentiable, we can directly learn to predict all intermediate outputs just using trajectory loss (8). An example of terrain learning with the trajectory loss is visualized in **Figure 9**. To make the training more efficient and the learned model explainable, we employ the geometrical loss (9) and terrain loss (10) as regularization terms. *stat*

The **Figure 11** show the prediction examples of the MonoForce model in diverse outdoor environments. From the example on the left, we can see that the model correctly predicts the robot’s trajectory and the terrain shape suppressing traversable vegetation, while the rigid obstacles (wall and tree logs) are correctly detected. The example on the right demonstrates the model’s ability to predict the robot’s trajectory (10 [sec]-long horizon) with reasonable accuracy and to detect the rigid obstacles (stones) on the terrain. It could also be noticed that the surfaces that provide the robot good traction (paved and gravel roads) are marked with a higher friction value, while for the objects that might not give good contact with the robot’s tracks (walls and tree logs) the friction value is lower.

We argue that the friction estimates are approximate and an interesting research direction could be comparing them with real-world measurements or with the values provided by a high-fidelity physics engine (e.g. AGX Dynamics [37]). However, one of the benefits of our differentiable approach is that the model does not require ground-truth friction values for training. The predicted heightmap’s size is  $12.8 \times 12.8\text{m}^2$  and the grid resolution is 0.1m. It has an upper bound of 1 [m] and a lower bound of  $-1$  [m]. This constraint was introduced based on the robot’s size and taking into account hanging objects (tree branches) that should not be considered as obstacles (**Figure 17**). Additionally, the terrain is predicted in the gravity-aligned frame. That is made possible thanks to the inclusion of camera intrinsics and extrinsics as input to the model, **Figure 6**. It also allows correctly modeling the robot-terrain interaction forces (and thus modeling the robot’s trajectory accurately) for the scenarios with non-flat terrain, for example, going uphill or downhill. This will not be possible if only camera images are used as input.

## IV. EXPERIMENTS AND RESULTS

### A. Dataset: ROUGH

We pre-train the terrain encoder on the large-scale outdoor dataset RELLIS-3D [47]. It is a multimodal dataset collected in an off-road environment containing accurately localized (with RTK GPS) 13, 556 lidar scans and corresponding time-synchronized RGB images.

Despite the amount and annotation quality of the data provided in the RELLIS-3D sequences, it lacks examples of a robot moving over hills, obstacles, and traversing high grass. To fill this gap in autonomous off-road navigation, a new Rugged Obstacles and Uneven Ground Hardcore (*ROUGH*) dataset will be released, containing sensory data from forest and field scenarios recorded with the two robot platforms: *MARV*, *Bluebotics Absolem*, **Figure 12**. It contains several hours of driving with the mid-sized robots in challenging terrain. The ultimate goal is to provide recordings of traversals on (or through) flexible natural obstacles like tall grass, hanging tree branches, mud, dense undergrowth, etc. The *ROUGH* sequences are collected with shape-changing tracked robots (**Figure 12**), which allows capturing a much larger range of dynamic responses - simply moving the auxiliary tracks changes the center and moments of inertia and the contact surface. To correctly utilize the effects of dynamics, *ROUGH* provides not only sensory data but also robot models with dynamic properties. The data set also contains carefully time-synchronized point cloud scans from Ouster OS0-128 lidar and corresponding RGB images from 4 Basler cameras installed on the robots (front, rear, left, and right). The robot localization data obtained using ICP SLAM [48] is also recorded. It was a better choice than GPS which is unreliable near or under tree canopy and close to buildings. The controls ( $\mathbf{u}$  in **Figure 6**) in the form of commanded tracks velocities and angles are recorded and used to train and evaluate the MonoForce model.

After training the MonoForce terrain encoder on the RELLIS-3D dataset, we fine-tune it on the *ROUGH* data sequences. Please note that the dataset is under construction

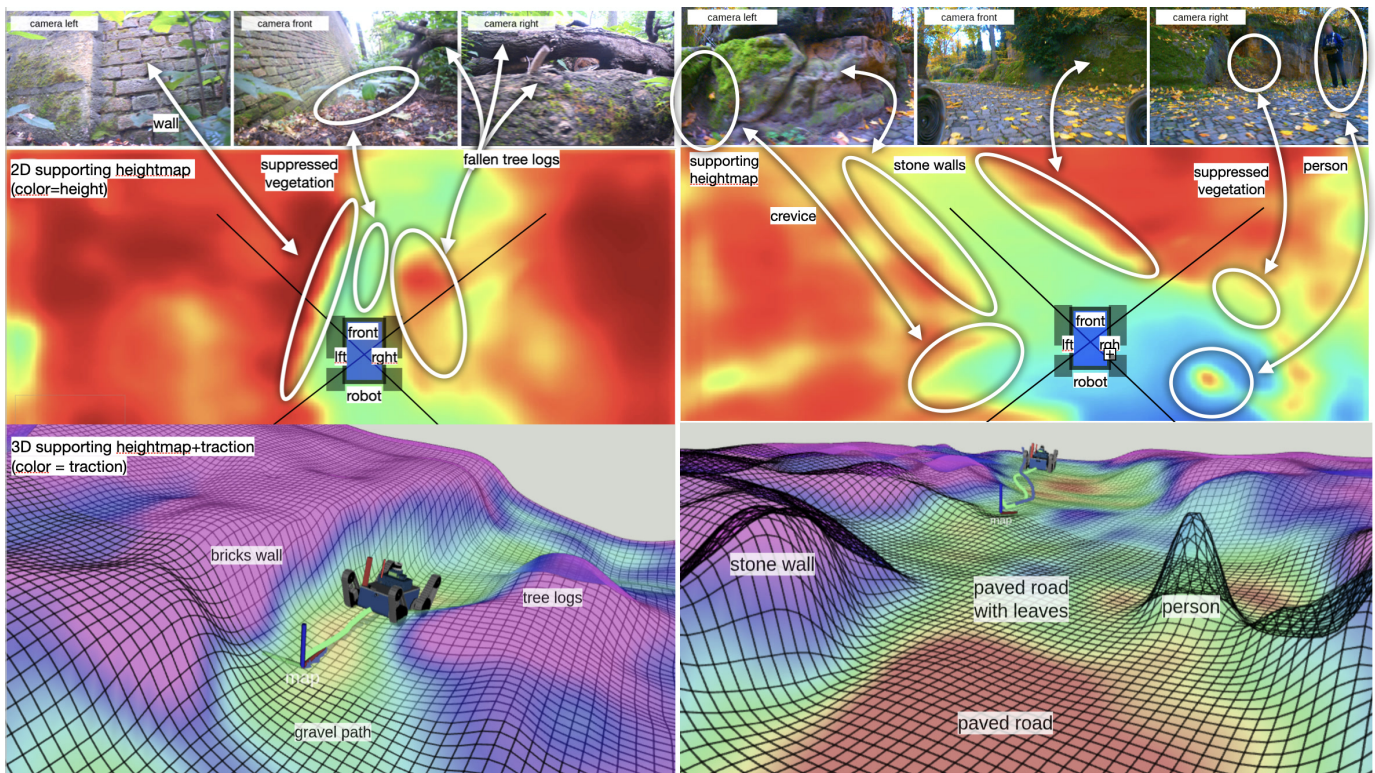


Fig. 11. **MonoForce prediction examples.** *Left:* The robot is moving through a narrow passage between a wall and tree logs. *Right:* The robot is moving on a gravel road with rocks on the sides. It starts its motion from the position marked with a coordinate frame and the trajectory is predicted for 10 [sec] using real control commands. The camera images are taken from the robot’s initial position (*top row*). The visualization includes predicted supporting terrain  $\mathcal{H}_t$  (*second row*). It is additionally shown in 3D and colored with predicted friction values (*third row*).



Fig. 12. **Two robot platforms** used to collect the ROUGH dataset. Notice that one platform has only four massive flippers, and the other has also two main tracks.

at the moment of writing and will be extended with the help of new robot platforms and data collection scenarios. The ROUGH dataset will be made publicly available<sup>2</sup>.

### B. Sensor Fusion

In this section, we study to what extent the inclusion of other sensor modalities (except for RGB images) improves terrain estimation accuracy. As we discuss in Section III-A, the terrain encoder model predicts terrain properties solely from RGB input. However, a natural question arises whether an additional point cloud input or a sensor fusion technique could improve the prediction. We adapt the architecture introduced in [22]

for terrain properties prediction. The modified BEVFusion architecture for the terrain prediction task from RGB and lidar inputs is provided in the Figure 13.

For different sensor inputs (multi-view RGB cameras and lidar), modality-specific encoders are applied to extract their features. Then the sensor-specific features are transformed into a unified BEV representation that preserves both semantic and geometric information. Following the [22] approach the convolution-based BEV encoder is applied next to the stacked BEV features to account for possible local misalignment between different sensors. The task-specific heads are added to predict different terrain properties (for example, its shape as a form of *heightmap* and *friction*) as shown in the Figure 13. The LSS [20] model is used as the camera input BEV-encoder, as described in Section III-A and the BEVFusion [22] paper. The VoxelNet [21] model is utilized as the point cloud input BEV-encoder. First, the raw point cloud input is voxelized into a 3D voxel grid. The point cloud coordinates are mapped to a discrete grid of binary indices (a value of 1 denotes that the voxel is occupied). Next, the 3D-convolution-based lidar Encoder processes the voxelized input to extract high-level feature representation. This operation is followed by max-pooling along the  $z$ -axis to reduce the 3D feature map to 2D BEV space.

We train and evaluate the LSS [20], VoxelNet [21], and BEVFusion [22] terrain encoders on the validation part of the ROUGH dataset (Section IV-A) following the procedure described in Section III-D. As the evaluation metrics, we use

<sup>2</sup><https://github.com/ctu-vras/rough-dataset>



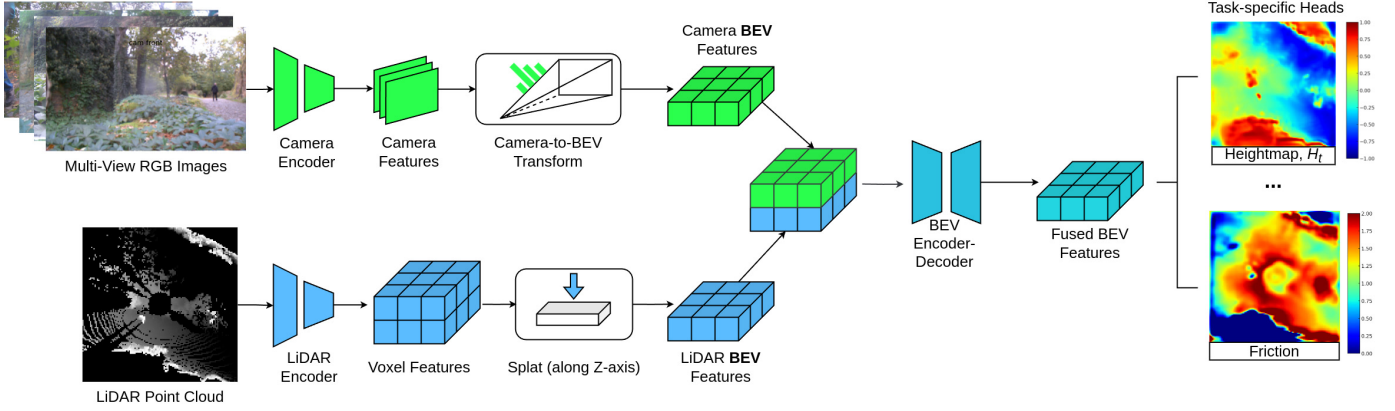


Fig. 13. **BEVFusion** [22] architecture. The model processes multi-modal inputs (RGB images and lidar point cloud) and fuses them into a shared bird’s-eye view (BEV) space. The LSS [20] architecture part is sketched in green (upper branch), while the model branch processing point cloud input (VoxelNet [21]) is depicted in blue. The fused BEV features are further used for terrain properties prediction tasks.

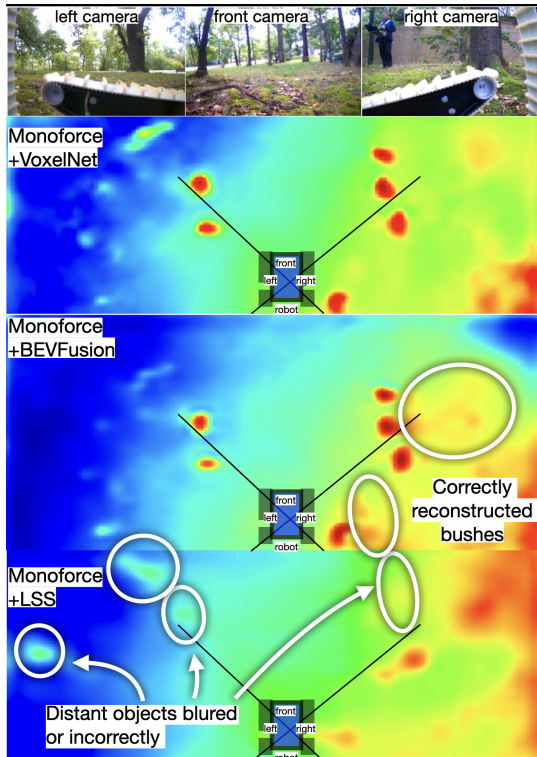


Fig. 14. The supporting terrain  $\mathcal{H}_t$  prediction with the LSS [20] (first row), VoxelNet [21] (second row), and BEVFusion [22] (third row) models. The predicted supporting terrain  $\mathcal{H}_t$  is projected onto camera images (as a point cloud) and visualized in the top-down view (on the right).

terrain prediction accuracy, Table I. The  $L_2$ -norms are computed to estimate geometrical,  $\Delta\mathcal{H}_g$  (9), and terrain,  $\Delta\mathcal{H}_t$  (10), heightmap prediction accuracy covering both geometric- and semantic- oriented tasks. The results in the two right-most columns of the Table I contain the terrain prediction accuracy metrics. The lidar input-based model (VoxelNet) performs better than the camera input-based LSS. However, the benefit of the sensor fusion on the terrain accuracy prediction is not obvious as the metrics  $\Delta\mathcal{H}_g$  and  $\Delta\mathcal{H}_t$  for both models (VoxelNet and BEVFusion) are nearly equal. The qualitative

results of the terrain properties prediction are visualized in Figure 14. It can be seen that although the LSS model provides a good estimate of the terrain shape (and thus the predicted trajectory matches the ground truth quite closely), it struggles to predict obstacles with sharp edges (tree trunks). The models that have a lidar input (VoxelNet and BEVFusion) provide more accurate terrain predictions. The BEVFusion prediction is also visualized in 3D in Figure 1 with the lidar point cloud input.

### C. Physics-based vs Data-driven Baseline

The following case study compares our hybrid physics-data-driven approach (Section III-B) to a purely data-driven method (Section III-C) in terms of trajectory estimation accuracy. We compare the physics model  $\nabla\text{Physics}$  introduced in Section III-B with the data-driven TrajLSTM network in terms of trajectory prediction accuracy. The following metrics are computed for qualitative evaluation on the validation part of the ROUGH dataset (Section IV-A):

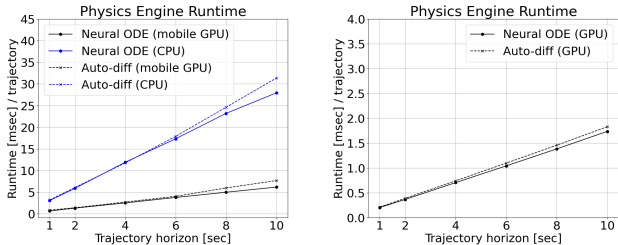
$$\Delta\mathbf{x} = \sqrt{\frac{1}{T} \sum_{t=0}^T \|\mathbf{x}_t - \mathbf{x}_t^*\|^2} \quad (11)$$

$$\Delta\mathbf{R} = \frac{1}{T} \sum_{t=0}^T \arccos \frac{\text{tr}(\mathbf{R}_t^\top \mathbf{R}_t^*) - 1}{2} \quad (12)$$

The (11) and (12) describe the predicted trajectory  $\{\mathbf{x}_t, \mathbf{R}_t\}$  translational and rotational errors respectively w.r.t. the ground truth  $\{\mathbf{x}_t^*, \mathbf{R}_t^*\}$ ,  $t \in \{0 \dots T\}$ . The ground truth poses were recorded using the SLAM method introduced in [48]. The results are summarized in Table I (columns  $\Delta\mathbf{x}$  and  $\Delta\mathbf{R}$ ) and Figure 5. Note that for the fair comparison, the TrajLSTM architecture is designed in a way that it has the same interface as the  $\nabla\text{Physics}$  module (takes the same input and yields the same output). This allows to use the  $\nabla\text{Physics}$  and TrajLSTM models interchangeably with different terrain encoder models (LSS [20], VoxelNet [21], BEVFusion [22]) that provide terrain estimates for the trajectory predictors. It can be seen from Figure 5 that the physics-driven trajectory predictor ( $\nabla\text{Physics}$ ) provides better trajectory prediction

TABLE I  
TRAJECTORY AND TERRAIN ESTIMATION ACCURACY.

input	method	terrain encoder	$\tau$ pred.	$\Delta\mathbf{x}$ [m]	$\Delta\mathbf{R}$ [deg]	$\Delta\mathcal{H}_g$ [m]	$\Delta\mathcal{H}_t$ [m]
RGB	hybrid	LSS [20]	$\nabla$ Physics ( <b>ours</b> )	0.062	2.042	0.1177	0.0896
RGB	data-driven	LSS [20]	TrajLSTM [19]	0.128	3.949		
point cloud	hybrid	VoxelNet [21]	$\nabla$ Physics ( <b>ours</b> )	<b>0.056</b>	<b>1.939</b>	<b>0.0987</b>	0.0774
point cloud	data-driven	VoxelNet [21]	TrajLSTM [19]	0.129	3.369		
RGB + point cloud	hybrid	BEVFusion [22]	$\nabla$ Physics ( <b>ours</b> )	0.068	1.966	0.0989	<b>0.0771</b>
RGB + point cloud	data-driven	BEVFusion [22]	TrajLSTM [19]	0.125	3.067		



(a) CPU: AMD Ryzen 7 4800H, (b) GPU: Tesla V100-SXM2-32GB, GPU: GeForce GTX 1660 Ti Mobile,  $N_{traj} = 2048$ ,  $N_{tra_j} = 512$

Fig. 15. The results are provided with the following configurations: grid resolution: 0.1 [m], number of robot body points: 223 (uniformly sampled with voxel size 0.1 [m]).

(both in translational and rotational components) regardless of the terrain estimation method. Additionally, for the data-driven trajectory predictor (TrajLSTM) we observe an impact of sensor fusion. The usage of BEVFusion terrain encoder helps to better estimate the translation and rotation of the robot w.r.t. its single-modality baselines (image-based LSS and lidar-based VoxelNet).

Overall, the point cloud input helps to predict terrain more accurately (Section IV-B and Table I) and the physics-based trajectory predictor  $\nabla$ Physics provides better results than its data-driven baseline TrajLSTM (Figure 5).

#### D. Physics Engine Computational Efficiency

The overall learning behavior (speed and convergence) is mainly determined by (i) the time horizon over which the difference between trajectories is optimized and (ii) the way the differentiable ODE solver is implemented. We compare further the computational efficiency of the two implementations of the differentiable physics engine: based on *Neural ODE* and *auto-differentiation*.

The Figure 15 shows the runtime of the differentiable physics engine depending on the predicted trajectories time horizon for the two solvers' implementation methods and different hardware configurations. The Figure 15 (a) shows the runtime on the standard laptop hardware (CPU and GPU), while the Figure 15 (b) shows the runtime on the high-performance GPU. It can be noticed that the runtime grows linearly with the time horizon in all cases and the laptop GPU implementation is around 5 times faster than the CPU one. The *Neural ODE* solver [45] is slightly more efficient

than the *auto-differentiation* one. For example, on a high-performance GPU (Tesla V100-SXM2-32GB), the prediction of 2048 trajectories (6 [sec]-long) takes around 1 [sec]. The short runtime of the differentiable physics engine allows for its efficient usage in the end-to-end learning pipeline (Section III-D) and for real-time trajectory shooting in navigation scenarios (Section IV-E).

#### E. Navigation in Unstructured Environments

Thanks to integration of the exteroceptive sensor to *Terrain Encoder* and GPU parallelization of the predicted trajectories (Section III-B), it is possible to use the MonoForce model for autonomous navigation in unstructured outdoor environments. In the navigation experiments, the robot is given a set of distant waypoints to follow. It is localized using the ICP SLAM method [48]. The MonoForce model runs onboard the robot's hardware and predicts terrain properties in front of the robot and a set of possible trajectories for different control commands. In the case of a tracked robot platform (Figure 12), the controls are the commanded velocities of individual tracks. A sample of predicted trajectories for given controls is visualized in Figure 18. To reach a goal safely, the robot chooses the trajectory with the smallest cost and distance to the next waypoint, Figure 17 Thanks to the MonoForce ability to predict robot-terrain interaction forces for a trajectory pose, it is possible to estimate the cost of each trajectory. We decide to calculate the cost as a values variance of reaction forces acting on the robot along a trajectory  $\tau$ :

$$C_\tau = \frac{1}{T} \sum_{t=0}^T \|\mathbf{N}_t - \bar{\mathbf{N}}\|, \quad (13)$$

where  $\mathbf{N}_t$  is the predicted reaction force acting on the robot at a time moment  $t$  and  $\bar{\mathbf{N}}$  is the mean value of the total reaction forces along the trajectory. Note that in the (13), we denote by  $\mathbf{N}_t$  the total reaction force acting on all robot's body points at a time moment  $t$ . The waypoint cost for a trajectory  $\tau$  is simply calculated as the Euclidean distance between the trajectory and the next waypoint:

$$C_{wp,\tau} = \min_{\mathbf{x} \in \tau} \|\mathbf{x} - \mathbf{x}_{wp}\|, \quad (14)$$

The total cost used for the trajectory selection in navigation is the weighted sum of the trajectory and waypoint costs:

$$C_{total} = \alpha C_\tau + \beta C_{wp,\tau}, \quad (15)$$

where  $\alpha$  and  $\beta$  are the hyperparameters for the trajectory and waypoint costs, respectively. With the described navigation

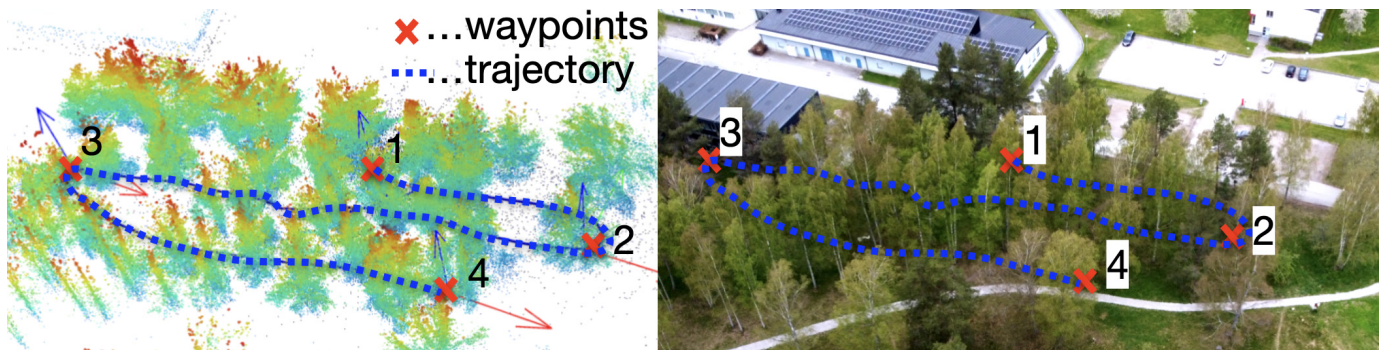


Fig. 16. The top-down view of the navigation experiment in the forest environment. During the experiment, the robot autonomously traverses the 260-meter-long path. The point cloud map construction (a) and robot’s localization were performed using the ICP SLAM method [48]

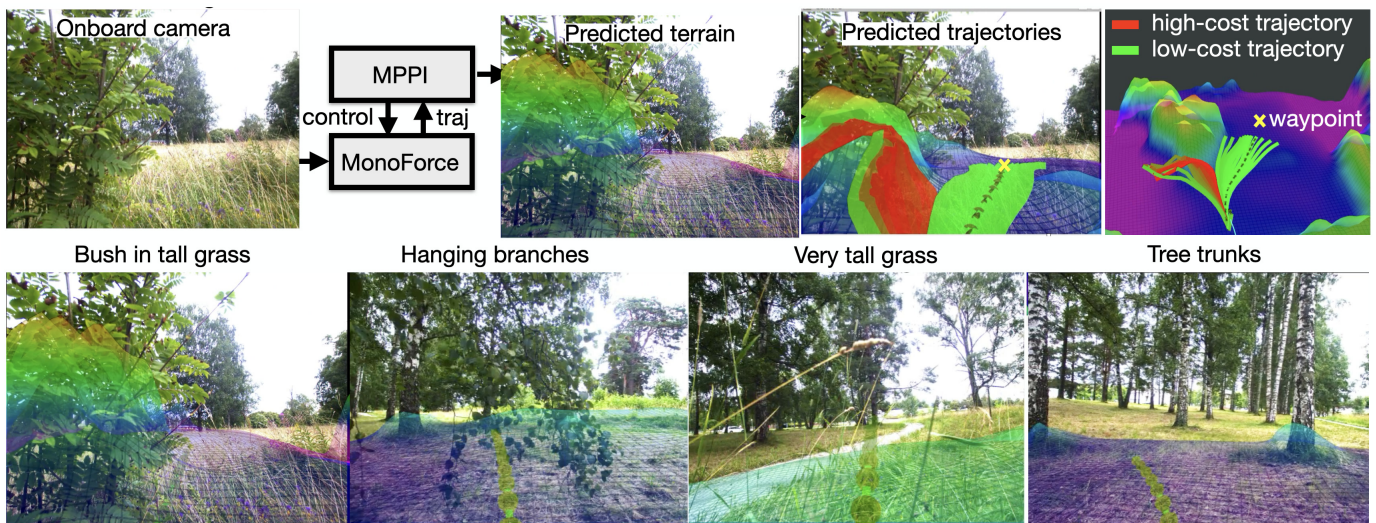


Fig. 17. Autonomous navigation in the forest environment with MonoForce. The robot follows a set of waypoints and at the same time avoids obstacles (trees, bushes, rocks, etc.). **First row (Control setup):** MonoForce prediction, based only on the onboard camera, includes terrain shape and a set of trajectories for different control commands sampled through a simplified MPPI technique. The colors of a possible trajectory correspond to the cost (red is the most expensive). The trajectory with green arrows is the one with the smallest total cost, (15). **Second row (Qualitative results):** Predicted supporting terrain and robot trajectory given camera images. The predictions and frontal camera images correspond to different time moments of the navigation experiment in the forest environment (Figure 16).

approach, the robot is able to autonomously navigate in the forest environment with uneven terrain, avoiding obstacles and following the set of waypoints, Figure 17. The Figure 16 shows the constructed point cloud map of the forest environment during the navigation experiment. It also contains an aerial photo of the forest area with the robot’s trajectory and the waypoints. The robot was able to autonomously navigate in the forest environment and traverse the 260-meter-long path.

## V. CONCLUSION

In this work, we have presented *MonoForce*, an explainable, physics-informed, and end-to-end differentiable model that predicts the robot’s trajectory from monocular camera images. As a *grey-box* model (physics-based and data-driven), it benefits from the end-to-end trainability in different domains while it still retains the determinism of its physics engine and explainability of its estimates of terrain properties. Thanks to the method’s end-to-end differentiability, it is possible to incorporate external sensor measurements in the training

pipeline. Additionally, due to the inclusion of the physics information, our model is able not only to generalize better (predict more accurate trajectories than data-driven baselines) but also provide interpretable intermediate outputs, for example *friction* and *robot-terrain interaction forces*. The training process is self-supervised; it only requires monocular camera images, lidar scans, and SLAM-reconstructed trajectories. The model learns to recognize non-rigid obstacles similar to those that have been driven over in the reference trajectories while keeping the understanding and prediction capabilities for obstacles it has not encountered yet. It treats them as rigid obstacles until future data prove otherwise.

In the experiments, we have shown that MonoForce generates accurate terrain heightmaps that in turn serve as a basis for robot-terrain interaction force and trajectory estimates. These estimates are valid both on rigid and non-rigid terrains. For terrain prediction, our results are comparable to the lidar-based methods (VoxelNet). We also study the benefits of sensor fusion on terrain estimation and robot-terrain interaction

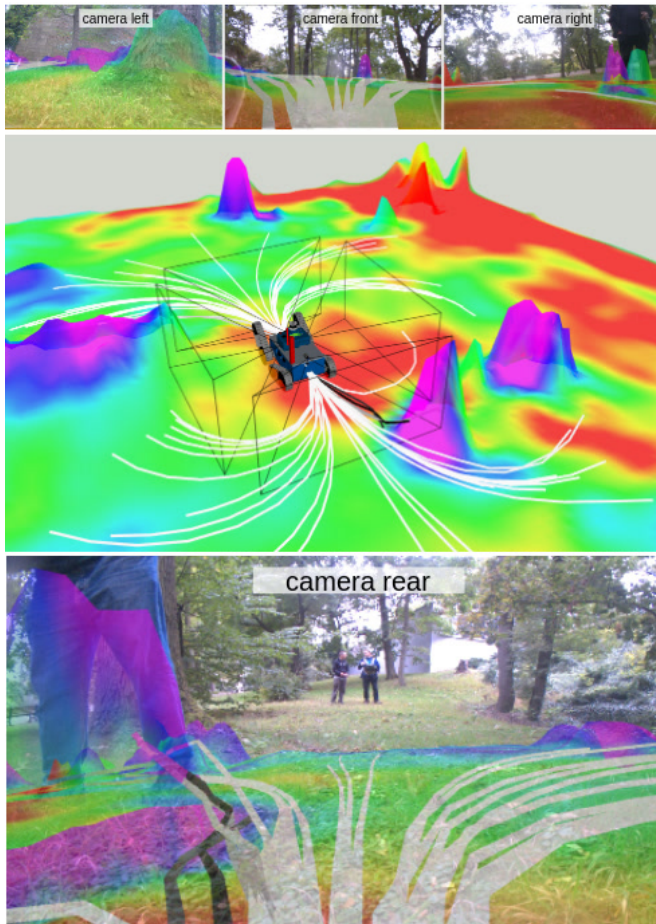


Fig. 18. MonoForce prediction projected to robot's camera images. The prediction includes supporting terrain  $H_t$ ; the colors correspond to the friction coefficient  $\mu$  (violet is low, red is high). A set of 64 trajectories for different control commands is visualized in white and black (low and high trajectory cost (13) respectively). The black frames denote the camera's field of view.

accuracy. It was shown that for data-driven approaches, the inclusion of other sensor modalities helps to predict the robot's trajectories more precisely. In addition, it was demonstrated that our physics-based approach ( $\nabla$ Physics) outperforms its data-driven baseline (TrajLSTM [19]) in terms of trajectory estimation accuracy.

#### ACKNOWLEDGMENTS

This work was co-funded by the Grant Agency of the CTU in Prague under Project SGS24/096/OHK3/2T/13, the European Union under the project Robotics and advanced industrial production (reg. no. CZ.02.01.01/00/22\_008/0004590), the Czech Science Foundation under Project 24-12360S.

#### REFERENCES

[1] S. Fabian, S. Kohlbrecher, and O. Von Stryk, "Pose prediction for mobile ground robots in uneven terrain based on difference of heightmaps," in *2020 IEEE Int. Symp. on Safety, Security, and Rescue Robotics (SSRR)*, 2020, pp. 49–56. 1

[2] S. Dogru and L. Marques, "An improved kinematic model for skid-steered wheeled platforms," *Autonomous Robots*, vol. 45, no. 2, pp. 229–243, 2021. 1

[3] A. Manoharan, A. Sharma, H. Belsare, K. Pal, K. M. Krishna, and A. K. Singh, "Bi-level trajectory optimization on uneven terrains with differentiable wheel-terrain interaction model," in *2024 IEEE/RSJ International Conference on Intelligent Robots and Systems (IROS) under review*, 2024, pp. 1–8. 1

[4] A. Loquercio, A. Kumar, and J. Malik, "Learning visual locomotion with cross-modal supervision," in *IEEE International Conference on Robotics and Automation (ICRA)*. IEEE, 2023, pp. 7295–7302. 1

[5] C. Niu, C. Newlands, K.-P. Zauner, and D. Tarapore, "An embarrassingly simple approach for visual navigation of forest environments," *Frontiers in Robotics and AI*, vol. 10, 2023. 1

[6] L. Wellhausen, A. Dosovitskiy, R. Ranftl, K. Walas, C. Cadena, and M. Hutter, "Where should I walk? Predicting terrain properties from images via self-supervised learning," *IEEE Robotics and Automation Letters*, vol. 4, no. 2, 2019. 1

[7] M. Guaman Castro, S. Triest, W. Wang, J. M. Gregory, F. Sanchez, J. G. Rogers III, and S. Scherer, "How does it feel? self-supervised costmap learning for off-road vehicle traversability," in *ICRA*, 2023. 1

[8] G. Kahn, P. Abbeel, and S. Levine, "BADGR: an autonomous self-supervised learning-based navigation system," *CoRR*, vol. abs/2002.05700, 2020. [Online]. Available: <https://arxiv.org/abs/2002.05700> 1

[9] A. Kumar, Z. Fu, D. Pathak, and J. Malik, "Rma: Rapid motor adaptation for legged robots," 2021. 1

[10] A. Kirillov, E. Mintun, N. Ravi, H. Mao, C. Rolland, L. Gustafson, T. Xiao, S. Whitehead, A. C. Berg, W.-Y. Lo, P. Dollár, and R. Girshick, "Segment anything," in *2023 IEEE/CVF International Conference on Computer Vision (ICCV)*, 2023, pp. 3992–4003. 2

[11] B. Amos, I. Jimenez, J. Sacks, B. Boots, and J. Z. Kolter, "Differentiable mpc for end-to-end planning and control," in *Advances in Neural Information Processing Systems*, vol. 31, 2018. 2

[12] W. Zeng, W. Luo, S. Suo, A. Sadat, B. Yang, S. Casas, and R. Urtasun, "End-to-end interpretable neural motion planner," in *The IEEE Conference on Computer Vision and Pattern Recognition (CVPR)*, 2019, pp. 8660–8669. 2

[13] J. Schulman, F. Wolski, P. Dhariwal, A. Radford, and O. Klimov, "Proximal policy optimization algorithms," *arXiv preprint arXiv:1707.06347*, 2017. 2

[14] F. Dellaert and M. Kaess, *Factor Graphs for Robot Perception*. Hanover, MA, USA: Now Publishers Inc., 2017. 2

[15] J. Moravec and R. Sara, "Robust maximum-likelihood on-line lidar-to-camera calibration monitoring and refinement," in *Computer Vision Winter Workshop*, 02 2018. 2

[16] A. Farea, O. Yli-Harja, and F. Emmert-Streib, "Understanding physics-informed neural networks: Techniques, applications, trends, and challenges," *AI*, vol. 5, no. 3, pp. 1534–1557, 2024. 2

[17] M. Macklin, "Warp: A high-performance python framework for gpu simulation and graphics," <https://github.com/ NVIDIA/warp>, March 2022, nVIDIA GPU Technology Conference (GTC). 3

[18] C. D. Freeman, E. Frey, A. Raichuk, S. Girgin, I. Mordatch, and O. Bachem, "Brax - a differentiable physics engine for large scale rigid body simulation," 2021. [Online]. Available: <http://github.com/google/brax> 3

[19] Y. Pang, N. Xu, and Y. Liu, "Aircraft trajectory prediction using lstm neural network with embedded convolutional layer," in *Proceedings of the Annual Conference of the PHM Society*, vol. 11. PHM Society Scottsdale, AZ, USA, 2019, pp. 1–8. 3, 6, 10, 12

[20] J. Pillion and S. Fidler, "Lift, splat, shoot: Encoding images from arbitrary camera rigs by implicitly unprojecting to 3d," in *Proceedings of the European Conference on Computer Vision*, 2020. 3, 4, 5, 8, 9, 10

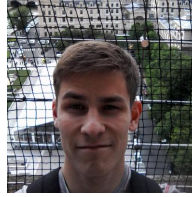
[21] Y. Zhou and O. Tuzel, "Voxelnet: End-to-end learning for point cloud based 3d object detection," in *Proceedings of the IEEE conference on computer vision and pattern recognition*, 2018, pp. 4490–4499. 3, 8, 9, 10

[22] Z. Liu, H. Tang, A. Amini, X. Yang, H. Mao, D. L. Rus, and S. Han, "Bevfusion: Multi-task multi-sensor fusion with unified bird's-eye view representation," in *2023 IEEE international conference on robotics and automation (ICRA)*. IEEE, 2023, pp. 2774–2781. 3, 8, 9, 10

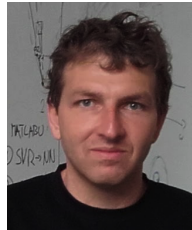
[23] K. Mani, S. Daga, S. Garg, S. S. Narasimhan, M. Krishna, and K. M. Jatavallabhula, "Monolayout: Amodal scene layout from a single image," in *The IEEE Winter Conference on Applications of Computer Vision*, 2020, pp. 1689–1697. 3

[24] J. Watson, M. Firman, A. Monszpart, and G. J. Brostow, "Footprints and free space from a single color image," in *Proceedings of the IEEE/CVF Conference on Computer Vision and Pattern Recognition*, 2020, pp. 11–20. 3

- [25] N. Hendy, C. Sloan, F. Tian, P. Duan, N. Charchut, Y. Xie, C. Wang, and J. Philbin, "Fishing net: Future inference of semantic heatmaps in grids," *arXiv preprint arXiv:2006.09917*, 2020. 3
- [26] J. Frey, S. Khattak, M. Patel, D. Atha, J. Nubert, C. Padgett, M. Hutter, and P. Spieler, "Roadrunner-learning traversability estimation for autonomous off-road driving," *arXiv preprint arXiv:2402.19341*, 2024. 3
- [27] D. E. Rumelhart, G. E. Hinton, and R. J. Williams, "Learning representations by back-propagating errors," *nature*, vol. 323, no. 6088, pp. 533–536, 1986. 3
- [28] S. Hochreiter, "Long short-term memory," *Neural Computation MIT-Press*, 1997. 3, 6
- [29] K. Cho, B. Van Merriënboer, C. Gulcehre, D. Bahdanau, F. Bougares, H. Schwenk, and Y. Bengio, "Learning phrase representations using rnn encoder-decoder for statistical machine translation," *arXiv preprint arXiv:1406.1078*, 2014. 3
- [30] G. Xie, A. Shangguan, R. Fei, W. Ji, W. Ma, and X. Hei, "Motion trajectory prediction based on a cnn-lstm sequential model," *Science China Information Sciences*, vol. 63, pp. 1–21, 2020. 3
- [31] Y. Yoon and K. Yi, "Trajectory prediction using graph-based deep learning for longitudinal control of autonomous vehicles: A proactive approach for autonomous driving in urban dynamic traffic environments," *IEEE Vehicular Technology Magazine*, vol. 17, no. 4, pp. 18–27, 2022. 3
- [32] X. Zou, J. Yang, H. Zhang, F. Li, L. Li, J. Wang, L. Wang, J. Gao, and Y. J. Lee, "Segment everything everywhere all at once," in *Thirty-seventh Conference on Neural Information Processing Systems*, 2023. [Online]. Available: <https://openreview.net/forum?id=UHBwFWIL> 4, 7
- [33] R. N. Yong, E. A. Fattah, and N. Skiadas, *Vehicle traction mechanics*. Elsevier, 2012. 3, 6
- [34] P. J. Blau, *Friction science and technology: from concepts to applications*. CRC press, 2008. 3
- [35] C. L. Simulations, "Vortex studio," <https://www.cm-labs.com>, 2025, version 2025.1 [Computer software]. 3
- [36] R. Serban, D. Negrut, A. Recuero, and P. Jayakumar, "An integrated framework for high-performance, high-fidelity simulation of ground vehicle-tyre-terrain interaction," *International journal of vehicle performance*, vol. 5, no. 3, pp. 233–259, 2019. 3
- [37] T. Berglund and M. Servin, "agxterrain," Algoryx Simulation AB, Umeå, Sweden, Tech. Rep. v. 1.01, March 2019. [Online]. Available: [https://www.algoryx.se/download/agxTerrain\\_tech\\_report.pdf](https://www.algoryx.se/download/agxTerrain_tech_report.pdf) 3, 7
- [38] P. Maheshwari, W. Wang, S. Triest, M. Sivaprakasam, S. Aich, J. G. Rogers III, J. M. Gregory, and S. Scherer, "Piaug-physics informed augmentation for learning vehicle dynamics for off-road navigation," *arXiv preprint arXiv:2311.00815*, 2023. 4
- [39] Z. Zhao, B. Li, Y. Du, T. Fu, and C. Wang, "Physord: A neuro-symbolic approach for physics-infused motion prediction in off-road driving," *arXiv preprint arXiv:2404.01596*, 2024. 4
- [40] R. Agishev, K. Zimmermann, V. Kubelka, M. Pecka, and T. Svoboda, "Monoforce: Self-supervised learning of physics-informed model for predicting robot-terrain interaction," in *2024 IEEE/RSJ International Conference on Intelligent Robots and Systems (IROS)*. IEEE, 2024, pp. 12 896–12 903. 4
- [41] R. Agishev, V. Kubelka, M. Pecka, T. Svoboda, and K. Zimmermann, "End-to-end differentiable model of robot-terrain interactions," in *ICML 2024 Workshop on Differentiable Almost Everything: Differentiable Relaxations, Algorithms, Operators, and Simulators*, 2024. [Online]. Available: <https://openreview.net/forum?id=XuVysF8Aon> 4
- [42] K. Bagi, "The contact dynamics method," in *Computational Modeling of Masonry Structures Using the Discrete Element Method*. IGI Global, 2016, pp. 103–122. 5
- [43] H. Pacejka, *Tire and Vehicle Dynamics*. Elsevier, 2012. 6
- [44] A. Paszke, S. Gross, and F. e. a. Massa, "Pytorch: An imperative style, high-performance deep learning library," in *Advances in Neural Information Processing Systems 32*, 2019, pp. 8024–8035. 6
- [45] M. N. Ricky T. Q. Chen, Brandon Amos, "Learning neural event functions for ordinary differential equations," in *ICLR*, 2021. 6, 10
- [46] F. Li, H. Zhang, P. Sun, X. Zou, S. Liu, J. Yang, C. Li, L. Zhang, and J. Gao, "Semantic-sam: Segment and recognize anything at any granularity," *arXiv preprint arXiv:2307.04767*, 2023. 7
- [47] P. Jiang, P. Osteen, M. Wigness, and S. Saripalli, "Rellis-3d dataset: Data, benchmarks and analysis," 2020. 7
- [48] F. Pomerleau, F. Colas, R. Siegwart, and S. Magnenat, "Comparing ICP variants on real-world data sets," *Autonomous Robots*, vol. 34, no. 3, pp. 133–148, 2013. [Online]. Available: <https://doi.org/10.1007/s10514-013-9327-2> 7, 9, 10, 11



**Ruslan Agishev** received his M.Sc. degree in Space and Engineering Systems from Skoltech, Moscow, Russia. He is currently pursuing a Ph.D. degree with the Faculty of Electrical Engineering, Czech Technical University in Prague, under the supervision of professor Karel Zimmermann. His research interests include active perception in robotics and physics-informed machine learning.



**Karel Zimmermann** is associate professor at the Czech Technical University in Prague. He received his PhD degree in 2008. He worked as a postdoctoral researcher with the Katholieke Universiteit Leuven (2008-2009) in the group of prof Luc van Gool. He serves as a reviewer for major journals such as TPAMI or IJCV and conferences such as CVPR, ICCV, IROS. He received the best lecturer award in 2018, the best reviewer award at CVPR 2011 and the best PhD work award in 2008. He was also with the Technological Education Institute of Crete (2001), with the Technical University of Delft (2002), with the University of Surrey (2006). His current research interests include learnable methods for robotics.